AMOEBA Polarizable Molecular Dynamics Simulations of Guanine Quadruplexes: from the c-Kit Proto-oncogene to HIV-1

Dina S. El Ahdab,[†,‡,¶] Louis Lagardère,[†] Zeina Hobaika,[†,‡] Théo Jaffrelot Inizan,[†] Frédéric Célerse,[†] Nohad Gresh,[†] Richard G. Maroun,[†,‡] and Jean-Philip Piquemal[*,†]

†*Sorbonne Université, Laboratoire de Chimie Théorique, UMR 7616 CNRS, 75005, Paris, France*

‡*Equipe Structure et Interactions des macromolécules, UR EGP, Centre d'Analyses et de Recherche, Faculté des Sciences, Université Saint-Joseph de Beyrouth, Beirut, Lebanon*

¶*Qubit Pharmaceuticals, 75014 Paris, France*

E-mail: jean-philip.piquemal@sorbonne-universite.fr

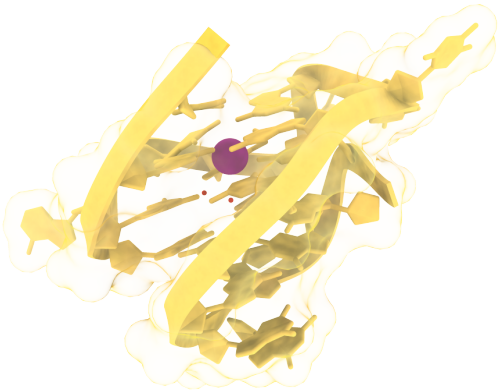

Abstract

We report extensive Molecular Dynamics (MD) simulations using the AMOEBA polarizable force field on two guanine quadruplex-forming oligonucleotides. The first system belongs to the *c-kit1* proto-oncogene, and the second to the LTR-III sequence of the HIV-1 retrovirus. For *c-kit1*, simulations were powered by an unsupervised adaptive sampling strategy, enabling a cumulated simulation time of 7.5 μs. If the stabilities of the three stacked core tetrads and the Long Propeller Loop were found to be consistent with previous MD studies performed with non-polarizable force fields, the present simulations exhibit some differences, especially concerning some nucleotides folding into an additional plan resulting in a further DNA stabilization. Therefore, the flexibilities of the two single-nucleotide loops and of one dinucleotide loop were analyzed by monitoring relevant inter-base distances, along with two key torsional angles, φ and γ, and the π-π stacking indexes. With the help of data analysis techniques and clustering algorithms, seven, well-defined, stable clusters could be identified. While remaining close in term of energy, their structural differences are caused by the small loops flexibility. Simulations performed starting from an empty channel demonstrated the importance of polarizable water molecules and their potential to replace the effect of cationic ions to stabilize the G-quad and prevent it from unfolding. Two stable druggable, 'cryptic', pockets were identified; the grooves of which could act as binding sites for pharmacological ligands. Subsequently, we extended our study to a preliminary 400ns conventionnal MD simulation on the HIV-1 LTR-III sequence where the stability of the guanine quadruplex was assessed and validated. Two cryptic pockets were additionally identified, but their conformations differed significantly from those observed in the *c-kit1* pockets. Among these two, only the first pocket was found to be potentially viable for ligand design.

Introduction

Guanine-Cytosine (GC)-rich long oligomer sequences are abundantly represented in oncogenes and retroviruses.[1,2] Their propensity to reorganize from double to quadruple helices was long recognized.[3,4] This occurs after strand separation and, in the G-rich strand, formation of stacked cyclic guanine tetramers involving well-defined G bases which can be distant in the primary sequence.[5] Such cyclic G tetramers were identified early on[6] and are stabilized by Hoogsteen pairing: each G has its O6 and N7 atoms accepting a proton from N1 and N2 of a neighboring G and in turn donates a proton from its N1 and N2 atoms to O6 and N7 of its other G neighbor.[6] A recurring motive in G-quadruplexes (GQ) is that of three stacked tetrads connected together by one or more nucleotide loops, as represented in figure 1. Alkali metal cations, mostly K^+ and Na^+, can be essential contributors to GQ stability. There are two cations located along the z axis of the two successive stacked tetramers, close to their geometrical centers. A third cation is located on top of one tetramer along this axis.[7,8] GQ's were early on recognized as targets for the design of chemotherapeutic ligands.[2] This is the case for human telomers which in cancer cells do not undergo shortening after each cell division, thus improving immortalization of these cells.[1] Such a shortening is prevented by the telomerase enzyme.[9] Thus its inhibition by high-affinity GQ-binding ligands could oppose immortalization.[1] GQ's are involved in the regulation of gene expression at the transcriptional and translational levels.[1] They are also found in the gene promoters of a wide range of genes that are essential in cell signalling, which modulates the six hallmarks of cancer.[10–13] We report in this work multi-μs polarizable molecular dynamic simulations bearing on two GQs, a human and a retroviral one, to unravel some distinct structural features and how they evolve in time. The first GQ is c-Kit, a proto-oncogene encoding for the Stem Cell Factor receptor CD117. CD117 is a tyrosine kinase receptor involved in intracellular signaling with consequences in differentiation, survival, adhesion, motility, angiogenesis and proliferation.[14] When mutated, CD117 can be responsible for several cancers, such as gastrointestinal stromal tumor (GIST), acute myeloid leukemia, and melanoma.[15] A tyrosine kinase (TK)

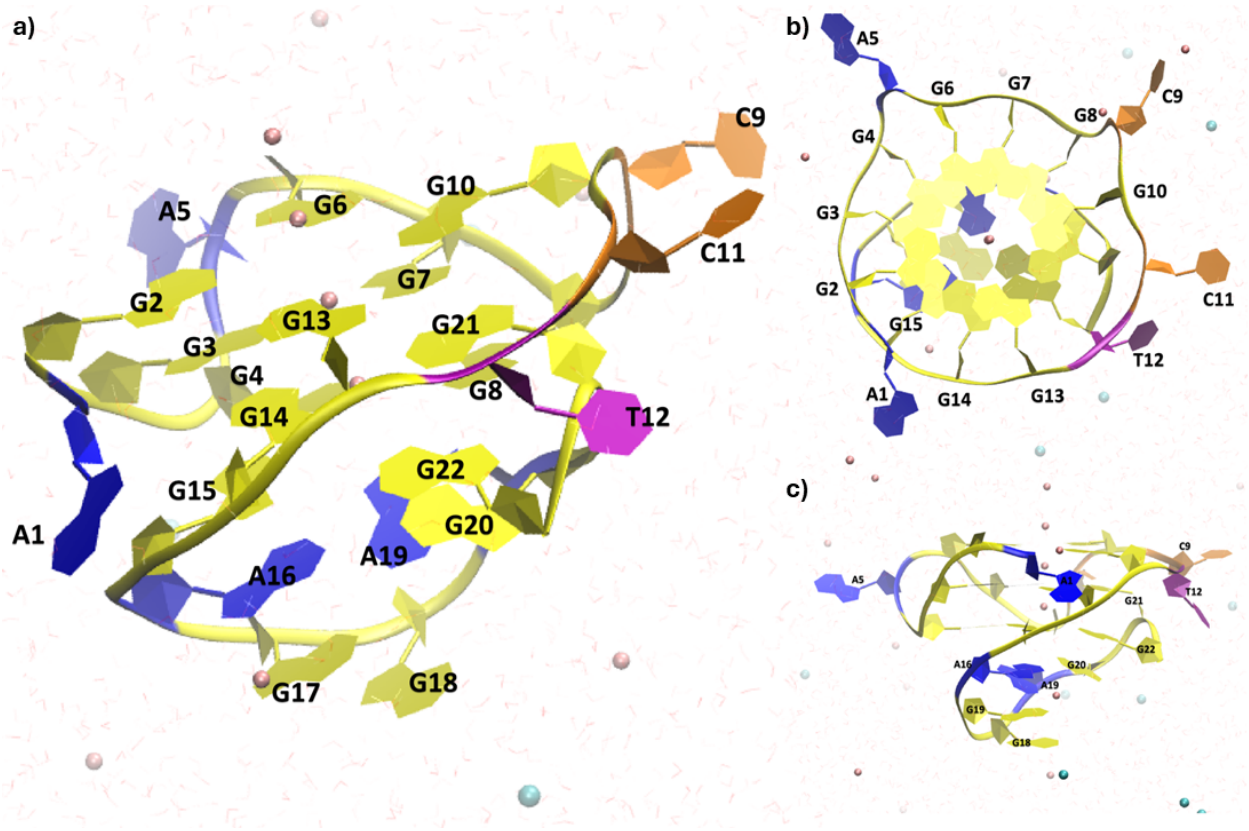

Figure 1: *c-kit1* GQ representation. *c-kit1* is formed by 3 G4 tetrad, one LP loop, 2 single nucleotide loops, one 2 nucleotides loop and a free nucleotide (A1). a) General representation showing all the nucleotides of *c-kit1* GQ. b) A top view showing organization of G nucleotides around the ionic channel. c) View from the side for a better visibility of the LP loop.

inhibitor, imatinib mesylate (Gleevec; Novartis Pharma AG, Basel, Switzerland), is effective for a majority of GIST patients.[16] However up to 33% of patients do not achieve optimal response due to a developing resistance against the inhibitor.[14,17]

Thus, interference with TK transcription at the genomic level could be attempted instead, such as by early stage inhibition of *c-kit1* transcription into CD117 mRNA.

Augmenting the stability of *c-kit1* proto-oncogene GQ by high-affinity ligands, by competing with its binding to the polymerase, could therefore constitute a novel transcription therapy against cancer.

We consider the *c-kit87up, 22-mer* sequence; d(AGGGAGGGCGCTGGGAGGAGGG), which is 87 nucleotide upstream of the transcription start site of the c-kit gene in human genome. It forms a single GQ species in K^+ containing solution.[18] The presence of four

tracts of three consecutive guanines separated by one up to four-residue linkers results into folding in a conventional parallel-stranded GQ structure. As shown in Figure 1, the first tetrad is formed by nucleotides G2, G6, G10 and G13. The second tetrad is formed by G3, G7, G14 and G21. The third is formed by G8, G14, G15 and G22. NMR and circular dichroism experiments showed the connecting linker sequences to be essential for GQ core stabilization.[18] These linkers are formed by five loops: two single-nucleotide loops with A5 and C9; one two-nucleotide lateral loop with C11 and T12 and one five-nucleotide long propeller-loop (LP) with A16, G17, G18, A19 and G20.

High-resolution structures of *c-kit1* GQ in the presence of K^+ are available from 3D-NMR spectroscopy (PDB code 2O3M) and X-ray crystallography (PDB codes: 3QXR, 4WO2, and 4WO3).[7,19,20] Since 4WO2 has the best crystallographic resolution for the 22-mer structure (1.82 Å) of human native c-Kit proto-oncogene promoter, it was selected as a starting structure for this study.

This study will be extended to G quadruplexes of the HIV-1 Long-Terminal Repeat 3 (LTR-III). While *c-kit1* lent itself to in-depth MD analyses in the context of classical potentials[8] and Drude polarizable potentials,[21] there are no precedents to our knowledge to MD simulations on any HIV-1 forming G-quadruplex. This preliminary extension could unravel similarities and differences between c-kit-1 and HIV-1 quadruplexes. G-rich sequences in the U3 promoter region of the HIV-1 Long Terminal Repeat (LTR) are shown to fold into a range of dynamically interchangeable G-quadruplex structures.[22–24] These sequences could act as silencing elements to regulate viral transcription. The stabilization of LTR GQ by GQ-specific ligands thus results into decreased viral production, with potent antiviral implications.

Among all GQs formed in the LTR sequence, LTR-III was shown to be the one giving rise to the richest conformational diversity *in vitro*. Thus, an NMR structure of LTR-III in K^+ solution, unraveled the following motives: a unique quadruplex–duplex hybrid consisting of a three-layer (3 + 1) GQ scaffold; a 12-nt diagonal loop containing a conserved duplex-

stem where six nucleotides are interacting by W-C hydrogen bonds to form a hairpin; a 3-nt lateral loop and a 1-nt propeller loop[21] (Figure 1).

Crystal and NMR structures could represent only some of the many substates and may not be the optimal ones for drug design. On the other hand, long-duration MD simulations could identify for both *c-kit* 1 and HIV-LTR-III alternative druggable conformations to those resolved by NMR or X-ray. Toward this aim the present study has several assets. The first is the recourse to the extension of the AMOEBA multipolar polarizable potential to nucleic acids,[25] enabling to reliably translate the stability conferred by the presence of two K^+ cations bound in the center of the two successive stacked G tetramers. AMOEBA parameters for nucleic acids have been refined through QM calculations and validated by MD simulations of DNA and RNA in water, as well as by crystal lattice simulations of classical and non-classical conformations.[25] Indeed, the use of polarizable force field has been shown for be particularly suited for complex and charged biological environments.[26–32] Worth mentioning in this connection is a recent validation study with the SIBFA polarizable potential[33]demonstrating that it is possible to closely reproduce the Quantum Mechanical (QM) energy profile for the channeling of alkali cations along the z axis of two stacked G tetramers[34] while this was not possible with non-polarizable force fields.[35]

Another asset is resorting, along with conventional MD (cMD), to large scale unsupervised adaptive sampling. We will in addition benefit from the GPU-accelerated implementation[36] of the Tinker-HP package[37] so that multi-μs MD simulations could be done in a considerably shortened time compared to conventional CPU simulations. Overstabilizing the quadruplex conformation of the *c-kit1* proto-oncogene could impair, at an early genomic stage, RNA polymerase-mediated initiation of transcription[1] This could enable to circumvent resistance to tyrosine kinase inhibitors which takes place at the later proteomic stage.

Unraveling the conformational behavior and temporal evolutions of c-kit G quadruplexes requires long simulation times. To achieve this, we will combine cMD with a rece,tly introduced unsupervised adaptive sampling strategy[29] which has been shown to greatly accelerate

the conformational sampling of the SARS–CoV–2 main protease[29,30] and Spike[32] proteins, offering the access to multi-μs MD simulations using GPUs. We will adopt a similar approach to enhance the sampling of the conformational space of GQs.

Our simulations will be compared with recent results obtained from non-polarizable MD using AMBER[8] and CHARMM C36,[21] as well as polarizable MD using the classical Drude oscillator model.[21] Regarding *c-kit1*, these comparisons now unveil previously unnoticed structural features. These include differences in clustering, the evolution of loops, responses to cations in the ionic channel and the emergence of alternative transient states.

Results and discussion

Conformational stability and transition states

Evolution of the stability of the different GQ *c-kit1* nucleotides

The root mean square deviation (RMSD) was calculated for all of the 7.5 μs of adaptive sampling trajectories in order to measure the average distance between the backbone atoms in the superimposed structures. It amounts to 3.5 Å for the whole GQ structure Figure 2 a), indicative of its overall stability. However, in order to follow the fluctuation dynamics of the different GQ components, the RMSDs for the GQ core, the LP loop and for the single nucleotide loops were calculated separately. Both the GQ core and the LP loop having RMSDs below 1 Å appear stable and structured. On the other hand, the single nucleotide loops have RMSDs fluctuating between 4 and 7 Å thus accountable for the whole structural dynamics.

The root mean square fluctuations (RMSF) were also calculated to search for the most dynamic c-kit-1 GQ bases. These were found to be single nucleotides A1, A5, C9, and dinucleotide C11-T12 (figure 2, b). It is thus the flexibility of these bases that most impacts the entire GQ dynamics. A better understanding of the dynamics of these nucleotides is

enabled by the corresponding temporal evolutions of two torsion angles, four distances and of the *pi–pi* stacking indices as reported below.

Evolution of the loop conformation

We have monitored the χ glycosidic torsion angle evolutions, with the possible occurrence of *(anti / syn)* base flipping.

The second monitored torsional angle is the angle γ governing the orientation of the sugar with respect to the phosphate backbone.

Figure 1 and Figure 2 in the SI represent a 2D plot of χ and γ angle fluctuations of A1, A5, C9, C11 and T12. C9 and C11 display large amplitudes of χ and γ variations compared to A1, A5 and T12. A1 and T12 have limited χ angle variations (-50° – +50° and +25° – +50° respectively) but have large γ angle fluctuations. Such fluctuations enable the formation of a transient Hoogsteeen base-pair above the first GQ tetramer involving G2, G6, G10, and G13. It is stabilized by two H-bonds, between HN6(A1) and O4(T12), and between N7(A1) and HN3(T12).

The involvement of N7 of A1 instead of N1 as in a standard W-C base-pair was unanticipated and appears to have no precedents from other GQ simulations.

It locates N7 of A1 in the same groove as the three G bases, G2, G3 and G4 on the same strand which form the three tetramers. By contrast, it is the formation of a W-C base-pair that was previously reported in the AMBER MD simulations.

This CMD simulation gave rise to the formation of a competing, longer-duration base-pair between A1 and C11.

The time evolutions of these two base-pairs were monitored. We considered first the initial CMD trajectory (800 ns), then trajectories resulting from adaptive sampling (7.5 μs).

Figure 3 reports the CMD evolutions of the HN6–O4 distance for A1–T12 and of the HN6–N3 distance for A1–C11. As shown in Figure 3, the first shortening of the first distance to app. 2 Å is enabled by the flip movement of T12 with large amplitude γ fluctuations, and

its stacking above the open face tetrad, particulary above G13 and G10. It first occurs after 80 ns but only lasts 1 ns. It occurs again between 180 and 220 ns. At 260 ns, the formation of the concurrent A1-C11 base-pair takes place and this base-pair lasts till the end of the CMD at 800ns.

Such a non-classical interaction was not previously reported in polarizable force field nor in non-polarizable force field studies simulations.[8,21] However, AMBER MD[8] did record a movement of C11 over the helix terminal along with a short-lived interaction with either T12 or the phosphate backbone of G10.

C9 and A5 remain highly dynamic and do not interact with any particular GQ nucleotide because of their locations in single nucleotide lateral loops.

Within the stable LP loop two stable interactions can be detected, namely between A16 and G20, and between G17 and A19. We have monitored the time evolutions of one relevant intermolecular distance, between A16(N1) and G20(HN1) and between G17(HN2) and A19(N1).

Such distances undergo only limited variations around 2 Å for A16–G20 and 2.15 Å for G17–A19, attesting to a lasting stability of the LP loop.

Such distances were recorded to vary between 2 and 3 Å respectively in AMBER MD.[8]

This result suggests that AMOEBA is able to detect and maintain non-classical interactions between nucleic bases. Their onset starts after 10ns. In contrast, an A1 flip movement was detected only after 2 μs in a MD simulation in the AMBER simulations.[8]

A1 is found to interact alternatively with G2 and G13, while C11 and T12 interact with G6 and G10. Since the behavior of highly dynamic loops shows flip movements from the X-ray conformation and π-stacking interactions with the open face tetrad, we calculated the stacking index of the four bases in order to unravel the bases involved in the stacking. G2 is thus found to interact with A1 while both C11 and T12 interact with G10, Figure 3,.

Thus the stability of A1 above the open face tetrad could be favored by two types of interaction : a short-lived Hoogsten base-pair (*cis* with T12 and a long-lived *anti* WC base-

pair with C11 together with a π-stacking interaction with G13 .

tICA clustering and cluster analyses

tICA is a dimensionality-reducing procedure.[38–41] It enables to identify microstates characteristic of the MD trajectories which result from the unsupervised adaptive sampling strategy. Such microstates are then regrouped into macro-states representative of each cluster. As exposed in our previous work,[29] DBSCAN is specially designed to identify clusters of arbitrary shape. Using two parameters: ϵ, the distance at which two points are considered neighbors, and *MinPts*, the minimum number of points necessary to define a cluster, DBSCAN unravels the existence of seven independent clusters, Figure 4. The free energies of each cluster can be evaluated along with its structural properties.

Such energies are computed through the evaluation of the probability distribution over the total number of structures. According to Figure 5 and Table 1 in the SI, cluster 1 has the lowest free energy thus the highest probability of existence. Cluster 5 ranks second with less than 1 kcal/mol higher free energy, the other clusters having 1.5-2.5 kcal/mol higher free energies. The RMSFs of the seven clusters enable to quantify their dynamics within the GQ. Figure 3 (SI) shows that nucleotide A1, single nucleotide loops A5 and C9 and dinucleotide loop C11-T12 undergo large fluctuations. Except for A5, these have unequal amplitudes in the clusters, in the range 6-9 ÅḂy constrast, the LP loop and the all twelve G bases of the GQ core undergo less than 2 Å variations. A1, A5, C9, C11 and T12 are thus identified by the RMSFs on the seven tICA-derived clusters as the most flexible nucleotides of *c-kit1* GQ, giving their individual shapes to the clusters. It is instructive to identify some of their key evolving structural features in these clusters. We have thus first considered the two above-mentioned torsion angles,χ and γ. Regarding χ angles, Figure 1 in the SI shows that all clusters share the same highest probability densities for A1, A5, C9 and T12. For C11, the χ fluctuations in cluster 1 are centered around a Gaussian function peaking at $\tilde{1}0°$. In the other clusters its χ fluctuations are centered around two major states with peaks in

two zones: -120°—170° and 120°–170°. Regarding γ angles, Figure 3 in the SI shows that all clusters have their highest probability densities for A1 and A5 centered around -25° and -110 ° respectively. Major differences between clusters are seen for C9, C11 and T12. The highest probability density for the C9 γ angle is located between 75° and 130° for clusters 1, 3, 6 and 7. Clusters 2, 4 and 5 have their peak at the same -40° value for this base. C11 is highly structured in cluster 6 but in cluster 1 its γ angle has two peaks, around -25° and 80°. In the other clusters, the γ probability density has shallow variations in two zones, the first between -100°—180° and the second between 100°–180°. For T12, γ peak around ~50° for clusters 1, 2, 4, 5 and 7 and around 60° for clusters 3 and 6. These results show that C11 can undergo continuous changes of its χ angle in the different clusters enabling it to populate both *syn* and *anti* states. By contrast, A1, A5 , C9 and T12 have χ centered around a single peak in all clusters. Regarding γ, both A1 and A5 show values centered around one single peak in all clusters. Both C9 and T12 show two predominant values, centered around -40° and 75°. Finally C11 has one peak in cluster 6, and two peaks in all other clusters.

Both conventional and adaptative MD have identified transient H-bonding interactions between N1 of A1 and HN3 of C11. However, the interactions between the N1 of A1 and HN3 ofT12 are not stable. The involved H-bonding distances were accordingly recomputed in the regrouped seven clusters (Figure 4 in the SI). We have recently resorted to the π-π stacking index[42] in an analysis of the M^{pro} SARS–CoV–2 protein. It has enabled us to quantify the extent of stacking between two residues, Phe140 and His163, a key interaction which stabilizes an oxyanion hole structure upon which the activity of each M^{pro} protomer depends.[29] Such an analysis could thus be pertinent in the present study, as it could similarly evaluate the stability of the stacking of A1, C11 and T12 above the first guanine tetrad. At the outcome of Adaptive MD, Figure 6, a), shows A1 to interact by π π-interaction with G13 in a persistent mode. This is shown by a high probability density for a stacking index of 0.2. Figures 6, b) and c) show that C11 and T12 stack above G10 preferentially than above G6. Thus on the one hand, the stacking index for C11–G10 of 0.15 has a much higher probability

density than the stacking index of 0.12 of C11–G6. On the other hand, the stacking index for T12–G6 is 0.10, smaller than for T12–G10 (0.18). The interest of clustering lies in the aim of being able to understand the various structural changes that may exist within each group of structures, thus allowing a better characterization of conformations in order to subsequently facilitate the design of future stabilizing molecules. These stacking indexes were similarly computed in the seven clusters in order to identify if different stacking arrangements could have occurred in these, resulting into alternative exposures of A1, G6, C11, and T12 to incoming ligands targeting them.

GQ stabilization by K^+ and polarizable H_2O molecules

Based on high-resolution X-ray crystallography, it was put forth that K^+ cations inside the channel exert an essential stabilizing role to the *c-kit1* promoter GQ. In order to study the *c-kit1* GQ behavior in the absence of these K^+ cations, we performed 20 independent simulations of 20ns each, starting from an empty ionic channel where we displaced the structural K^+ coordinates outside of the GA structure and to join the bulk ions.

We assessed the stability of the GQ structure by calculating its RMSD in each trajectory. Figure 5 in the SI shows clearly that *ckit1* GQ preserved its stability and initial conformation during all 20 trajectories with some minor conformational changes of the unengaged free nucleotides (A1, C11 and T12). GQ core stability can be explained by the fact that the ionic channel was never seen empty by the end of any of these MD simulations. We counted the number of H_2O molecules and K^+ cations inside the ionic channel for every frame of these 20 MD simulations to understand the process of the ionic channel filling. To do so, we defined a virtual sphere centered on the mass center of the 12 Guanines contributing to the formation of the *ckit1* GQ core and with a radius of 4 Å (which is the best radius to cover all and only the ionic channel). As it is shown in Figure 7, and more in details in Figure 6 in the SI, several scenarions of the ionic channel filling can be possible.

The highest frame density detected refers to the presence of 1 H_2O molecule and 1 K^+

cation inside the ionic channel.

The second highest density corresponds to an empty channel where no H_2O molecules, nor cations are detected inside the GQ core. We recall that no channel is empty at the end of any of the 20 MD simulations and the density here corresponds to the frames from the beginning of the trajectories in which the ionic channel is empty. All *ckit1* GQ ionic channel start to be fulfilled after a while from the beginning of the MD simulations.

The third highest density observed, corresponds to 2 H_2O molecules and 1 K^+ cation that can be present inside the ionic channel. To a slightly lower density, we can observe either the presence of 2 H_2O molecules, either 1 H_2O molecule only.

Once the channel is thus filled, all loops evolve in the same fashion as in the initial MD simulations with two K^+ cations present since their start with no significant relative structural changes. We calculated the average dipole moments of the H_2O molecules that have entered the channel. Their mean value : 2.72 D is slightly below the 2.78 D AMOEBA value computed for liquid H_2O. This, albeit modest, decrease could possibly be due to a local decrease of the polarizing guanine-induced field inside the channel, due to the mutually-opposing fields exerted in each tetramer by the two pairs of two symmetry-related guanines. In this connection, it was recently observed[30] that a dense and a compact environment generates a global many-body depolarizing effect influencing the H_2O molecule induced dipoles. CHARMM simulations resulted into one K^+ from the solvent phase entering the channel after 20ns.[21] This entrance was from below tetrad 3 rather than, as in AMOEBA MD, from above tetrad 1. It reached tetrad 3 after transiting through the Long Propeller Loop, which as mentioned in,[21] could cause transient conformational distorsions in the LP loop and tetrad 3. Drude simulations,[21] starting from an empty channel, resulted into one K^+ transiently interacting with T12 and then entering the GQ core through the first tetrad, as found here in the present work. The additional advantage AMOEBA is bringing here, is its capacity to show that even if K^+ cations are not entering the ionic channel, GQ can still be perfectly maintained thanks to the entry of water molecules.

Cryptic Pockets

Could potential drug binding cavities be detected in any of the seven identified clusters? We have resorted to the DoGSite Scorer software,[43] an automated 'cryptic' pocket descriptor. For all seven clusters, two pockets could be defined: P1, formed by bases A1, G2, G3, G13, G14, G15, A16, and P2, formed by bases G7, G8, C9, G10, C11, G21 as shown in Figure 8.

Could in these pockets some key inter-base distances persist throughout adaptive MD, and how do their values compare in the seven clusters?

We have considered three pairs inside P1: G3–G15, G2–G14 and A1–G13 and two pairs inside P2: G21–G8 and G10–G7. In the G–G pairs, the first G belongs to one tetrad and the second to the following tetrad. It is stacked below the guanine that donates two H-bonds to the first G. The intermolecular distances which we monitored are between N7 of the first G and HN1 of the second. In the A–G pair, the corresponding distance is between N7 of A1 and HN1 of G13 which is part of the first tetrad. This choice of G–G distances should enable to evaluate if partial unstacking of the quadruplexes or distortion of the GQ H-bonding could have occurred during MD.

Figure 7 in the SI shows that in all seven clusters, for each G–G pair, such distances remain closely distributed around sharp peaks in a 4 - 4.5 Å interval. This attests to the stability of the GQ core in all clusters. It should favor the binding of an incoming ligand to the groove formed by the bases belonging to P1 or to P2. By constrast, the distance A1–G13 is seen to undergo large fluctuations in all clusters, notably in clusters 5 and 7. This is clearly caused by the large-amplitude motion of A1, whose RMSF exceeds 9 Å in these two clusters.

Extension to LTR-III region of HIV

We have performed a preliminary extension of AMOEBA to the LTR-III region of HIV which is also prone to GQ-formation. At this stage, we performed a 400 ns CMD using a high-resolution NMR structure as a starting point (PDB ID : 6h1K). The DoGSite Scorer

software[43] could detect two cryptic pockets: P1, formed by bases G2, A4, G5, G6, G8, T9, G11, C12, C13, T14, G15 and G19 and P2 formed by bases G1, G2, G3, G15, G19, G20 and G21. P1 is mainly located in the hairpin domain while P2 is located in the upper face of GQ domain (Figure 9 a and b)). Similar to *c-kit1* GQ, RMSD and RMSF calculations (Figure 8,a and 8,b respectively in the SI) attest to a highly structured GQ core. By contrast, the hairpin domain, and both the three-nucleotide and the single-nucleotide loops are unstructured.

As reported above for *c-kit1*, we have monitored representative inter-base distances inside P1 and P2. In P1, we have considered the three W-C base pairs A4–T14, G5–C13 and G6–C12. In P2, the two bases are G2–G19 and G1–G20. For the A–T base pair, the distances are between H3N(T) and N1(A). For the two G–C base-pairs, they are between H1N and N3. In P2, for both G2–G19 and G1–G20, they are between the O6 atoms of the two bases. This choice, rather than the one done for *c-kit1*, was motivated by the different glycosidic angles of the consecutive bases: anti for G2 and G20, and *syn* for G1 and G19. This results into the N7 atoms of two consecutive bases located on opposite strands. The O6-O6 distances were considered to be less sensitive to the alternation of the glycosidic angles. By contrast, all GQ core guanines in c-kit are anti.

The distance probability density functions (Figure 8, c in the SI)) attest to a larger stability of P2 than P1. It is thus observed that the two O6-O6 distances in P2 are clearly centered around two peaks in a 4.5-4.8 Å interval. In P1, the A4-T14 distance has two peaks. The first corresponds to a standard W-C H-bond distance, but the second at 4.2 Å corresponds to a dissociated pair. For G6-C12, similarly, there are two peaks, the first at 2.0 Å corresponding to a W-C base-pair, and the second at 4.0 Å corresponding to a dissociated base-pair. For G5–C13, a shallow evolution is found in the 2.0 – 4.5 Å range. This should have clear implications regarding the design of LTR-III ligands, which should target P2 rather than P1.

Perspectives

The DoGSite Scorer software[43] unraveled two 'cryptic' pockets within *c-kit1* GQ, P1 and P2, which could serve as 'druggable' sites for potential pharmacological ligands. Figure 8 a) gives a representation of the accessible surface of P1, clearly revealing the existence of a 'groove' for their binding.

Along these lines, we have in a preliminary approach extended this study by a 400 ns CMD on another GQ-forming oligonucleotide, that of the LTR-III of HIV-1. At its outcome, DoGSite Scorer identified two cryptic pockets, P1 and P2, of which only P2, with limited RMSD variations, could possibly be used as a druggable ligand binding site. Figure 9 gives a representation of the accessible pockets.

On the basis of such results, we have initiated in our Laboratories the design of novel ligands targeting the grooves of cryptic pockets P1 and P2 of *c-kit1*, and of P2 of the LTR-III of HIV-1. This is done closely following the procedures leveraged in the present work, and the results will be reported in due course. It is also planned to extend such studies to other G-forming quadruplexes from other oncogenic and retroviral sequences.

Conclusions

We have performed long AMOEBA polarizable MD simulations on two guanine quadruplexes. The first is formed within an GC-rich oncogenic sequence, associated with the *c-kit1* oncogene, and the second is found within a Long Terminal Repeat of the HIV-1 retrovirus.

We first focused on a 22-mer oligonucleotide belonging to the *c-kit1* oncogene, the overexpression of which can lead to cancer. This oligonucleotide can fold into guanine quadruplexes, a conformational change occurring during DNA transcription into CD117 mRNA. Understanding the dynamics of this 22-mer oligomer in its quadruplex is essential and was analyzed in detail.

This study has benefitted from several assets. An essential one is the use of AMOEBA

polarizable force field that was recently made available for nucleic acids.[25] A second one is the availibility of the GPU-acceleration[36] available in the Tinker-HP software[37] that enabled to performed enhanced sampling simulations via an unsupervised adaptive approach.[44] In total, we achieved an aggregated c-kit1 simulation time of 7.5 μs.

Most simulation features were found to be fully consistent with those previously obtained with the non-polarizable AMBER[8] or polarizable Drude[21] force fields. Nevertheless, some differences were found. If the long-duration stability of the GQ core, made of three stacked guanine quadruplexes, and that of the Long-Propeller Loop observed in previous studies were confirmed, this contrasts with the high dynamics of the single-nucleotide loops A5, C9 and of the dinucleotide loop C11-T12, whose mobilities impact the whole dynamics of the *c-kit1* 22-mer. Such mobilities were evaluated in the individual clusters in terms of: a) :H-bonding distances in base-pairs A1-T12 and A1-C11, A16-G20, and G17-G20; b): the Two torsion angles, i.e. the glycosidic χ and the γ angles of bases A1, A5, C9, C11 and T12, and c): The π-stacking index between A1 and both bases, C11 and T12 of the dinucleotide loops, and a G base of the nearest guanine tetrad, monitored the evolution in the course of adaptive MD for base-pairs A1-G2, A1-G13, C11-G6, C11-G10, T1-G6, and T12-G10. The tICA analyses revealed 7 distinct clusters transiently stabilized during the MD simulations based on PC1 and PC2. Available X-ray structures were identified in the largest detected cluster confirming the GQ core stability. The fact that the identified clusters remain closely related in terms of energy is due to the different conformations of the single and dinucleotides loops. However, all these clusters share the same stable cryptic pockets that can be therefor considered as potentially druggable sites for drug discovery. Empty channel simulations demonstrated the importance of polarizable water molecules and their potential to effectively replace the effect of cationic ions to stabilize the GQ, preventing it from unfolding as oberved in non polarizable force field simulations, highlighting the interest of using the AMOEBA in these cases.

Our modeling strategy was extended to another model and thus was tested on the LTR-III

region of HIV. The stability of the G-Quads was also assessed and validated. Well-defined stable cryptic pockets were also detected. One of them could be exploited as druggable site for future drug discovery studies.

Technical Appendix

Materials And Methods

System Construction

The starting structure for *c-kit1* GQ was taken from the crystallography structure in PDB entry *4WO2*.[20] The structure was solvated in a water cubic box with dimensions of 60 Å. To mimic physiological conditions, 150 mM of [KCl] (K^+, Cl^-) was added to the system. The system was then minimized with the AMOEBA polarizable force field[25,45,46] using L-BFGS algorithm until a Root Mean Square (RMS) gradient of 1 kcal/mol was reached.

Conventional Molecular Dynamics

The MD simulations were performed using the recently developed GPU module[36] of the Tinker-HP software,[37] which is part of the Tinker 8 platform.[47] This newly developed module efficiently leverages mixed precision,[36] offering a substantial acceleration of simulations. The assembly was equilibrated for 1ns at each of the following temperatures successively: 50, 100, 150, 200, 250, and 300K. The Smooth Particle Mesh Ewald[48] was used with the Ewald and van der Waals cutoffs set to 7 Å and 9 Å, respectively. The MD simulations used the BAOAB-RESPA integrator with a 2 fs outer timestep, a Bussi thermostat, hydrogen-mass repartitioning (HMR), and random initial velocities. Smooth Particle Mesh Ewald (SPME) method was used for handling periodic boundary conditions with a grid of dimensions 60 Å x 60 Å x 60 Å. The production phase was conducted at 300 K for 800 ns for c-kit and 400 ns for HIV-1 LTR-III.

Unsupervised Adaptive Sampling Strategy for Conformational Exploration

Adaptive sampling has proven to be a powerful exploration tool for studying protein folding and dynamics, as well as for exploring a diversity of rare molecular events.[49–52] Recently, we developed a new fully unsupervised Adaptive Sampling strategy that enables the simultaneous use of hundreds of GPU cards.[29] The method divides the simulation procedure into iterations, each composed of a swarm of independent MD simulations run in parallel.

At the beginning of each iteration, some initial structures are selected from the structures sampled in past iterations. The selection procedure is mathematically designed to fully explore a low-dimensional space of slow variables generated by dimensionality reduction algorithms such as PCA and tICA.

From these selected structures, independent MD simulations are run in parallel, potentially combined with other enhanced sampling methods,[53] to generate new structures that can serve as starting points for future iterations.

In this particular case, we first ran an initial 800 ns of cMD where we selected 50 starting point structures using the Adaptive Sampling algorithm in the four-dimensional PCA space. The choice of 50 starting points is heuristic, as we have observed it to be sufficient for efficiently sampling the conformational space of a protein of similar size: the SARS–CoV–2 protein. The number of dimensions for the PCA space is determined based on the fact that the other PCA dimensions have negligible variance contribution below 4 %. Each cMD simulation sampled 15 ns, and these simulations were performed in the NVT ensemble at 300 K. Thus, with a total of 10 iterations, we generated more than 7.5 μs of simulation."

Time-structure Independent Component Analysis

Time-structure Independent Component Analysis (tICA) was introduced into MD as a method to extract slow collective variables.[38,39] tICA solves a variational approach by which

it finds an optimal approximation to the eigenvalues and eigenfunctions of the Markov operator underlying the molecular dynamics data.[38,40,41] As a result, tICA is ideally suited for clustering and to prepare data for Markov models.

In fact, tICA followed by clustering techniques makes it possible to classify the structural and physico-chemical properties of the structures within an MD trajectory. Additionally, this approach reveals valuable insights into the system's behavior over time.

While tICA shares similarities with PCA, it offers notable advantages for capturing the dynamics of proteins. Unlike PCA, which relies on static and linear properties, tICA aims to create independent components as meaningful as possible to better describe the dynamics of a system.[54] This makes tICA a more suitable choice for our analysis.

Throughout the simulations, with tICA and clustering techniques we identified distinct clusters for each of the variants analyzed. We organized the final MD trajectories into clusters based on the eigenvalues and eigenfunctions of the covariance matrix.

By employing this classification approach, we can observe similarities between the macro-states of each variant, enabling us to discern common structural or dynamic changes shared among the variants.

A classification makes it possible to observe the similarities between the macro-states of each of the variants to discern a structural or dynamic change to them.

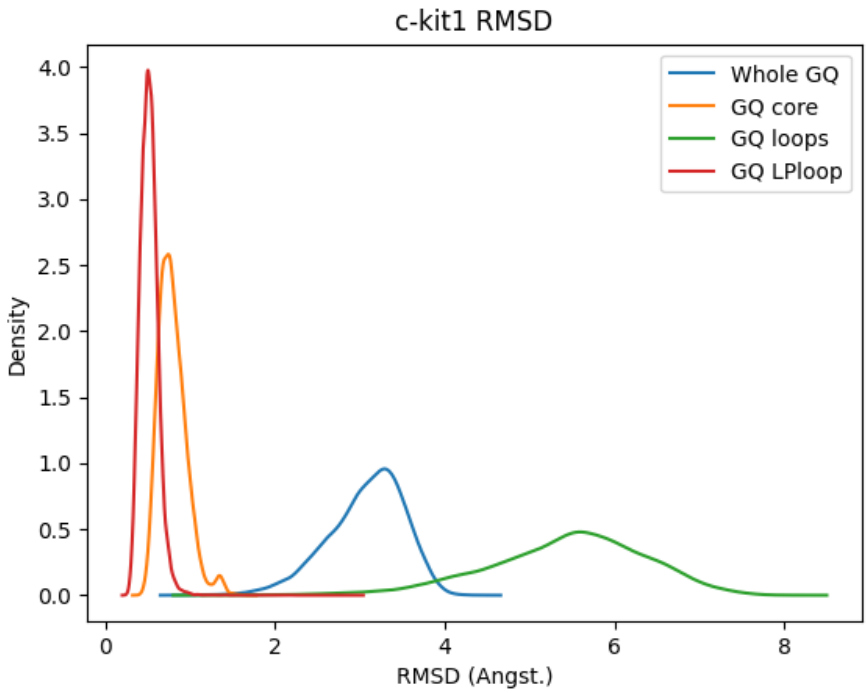

a)

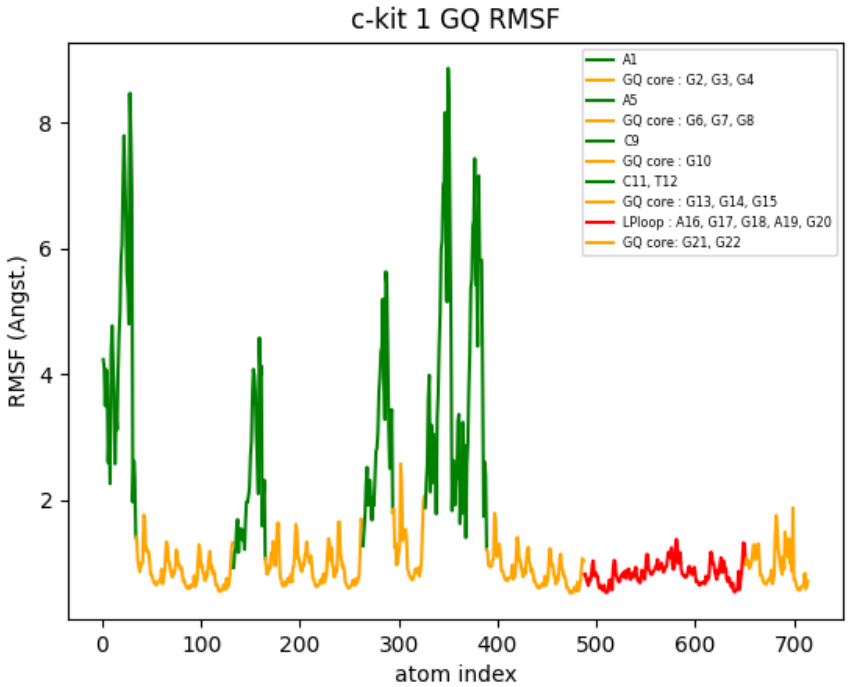

b)

Figure 2: RMSD and RMSF of *c-kit1*. For the RMSF, the atom indices of nucleotides A1, A5, C9, C11 and T12 are respectively : 0 to 33, 133 to 164, 133 to 164, 133 to 164 and 133 to 164.

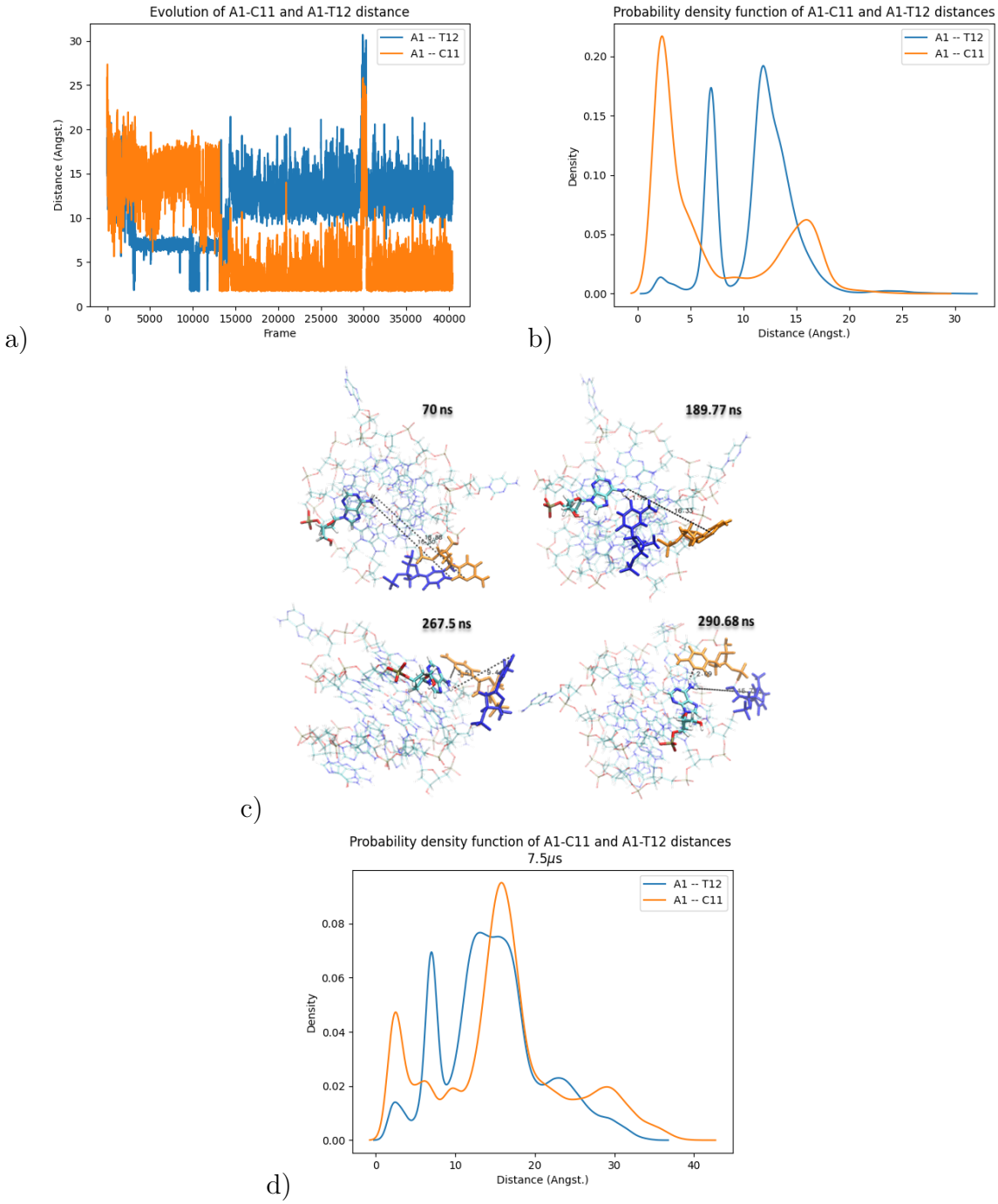

Figure 3: Evolution of the distance between A1(H) and T12(O) shown in blue and between A1(H) and C11(O) shown in orange. 5000 frames correspond to 100 ns simulation time. c) Representation of four structures at four different times of the CMD trajectory showing the evolution of distances A1–T12 and A1–C11.

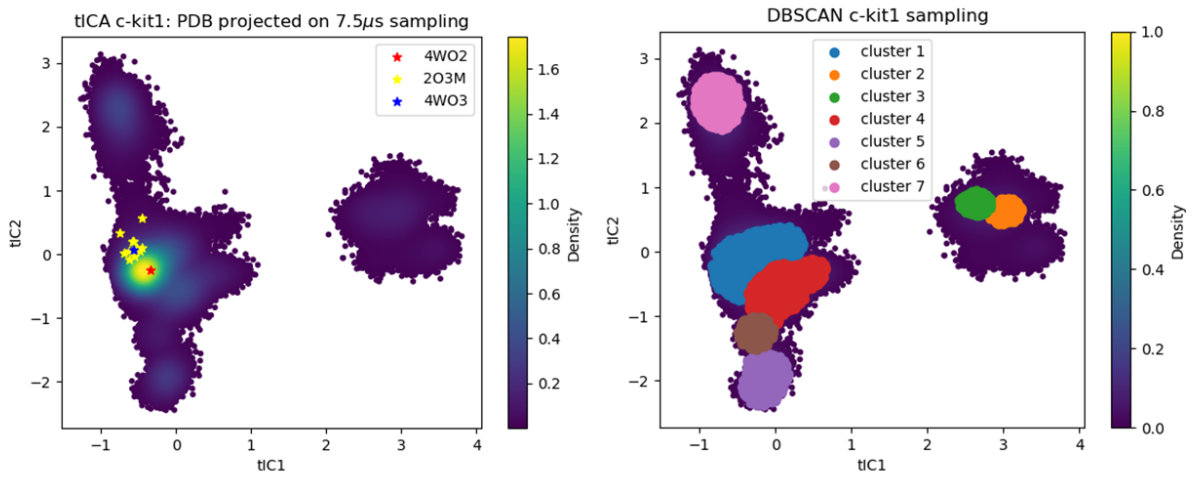

Figure 4: tICA DBSCAN sampling and clustering

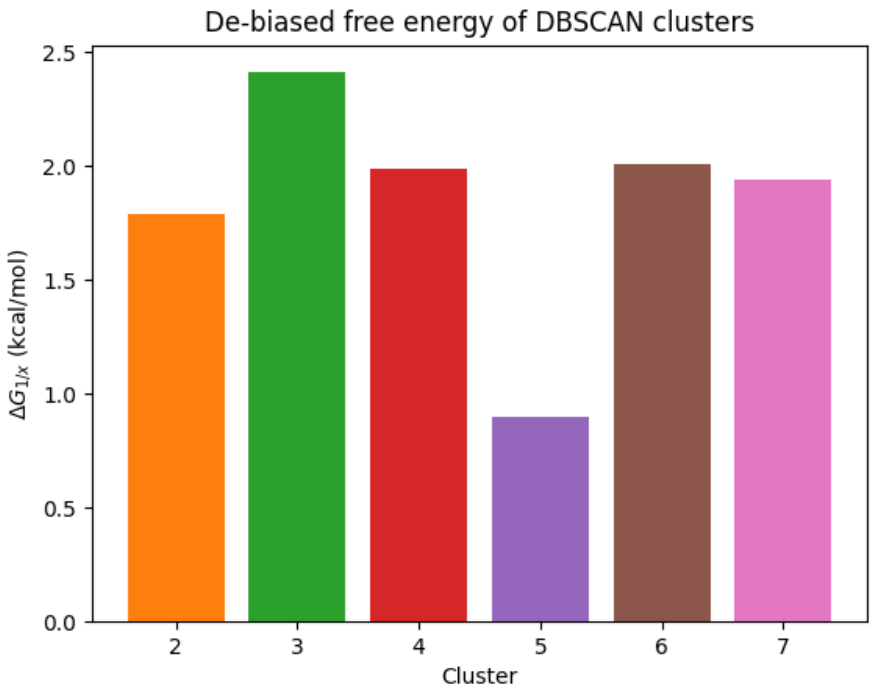

Figure 5: Relative free energies of the DBSCAN 7.5μs tICA clusters, with respect to cluster 1.

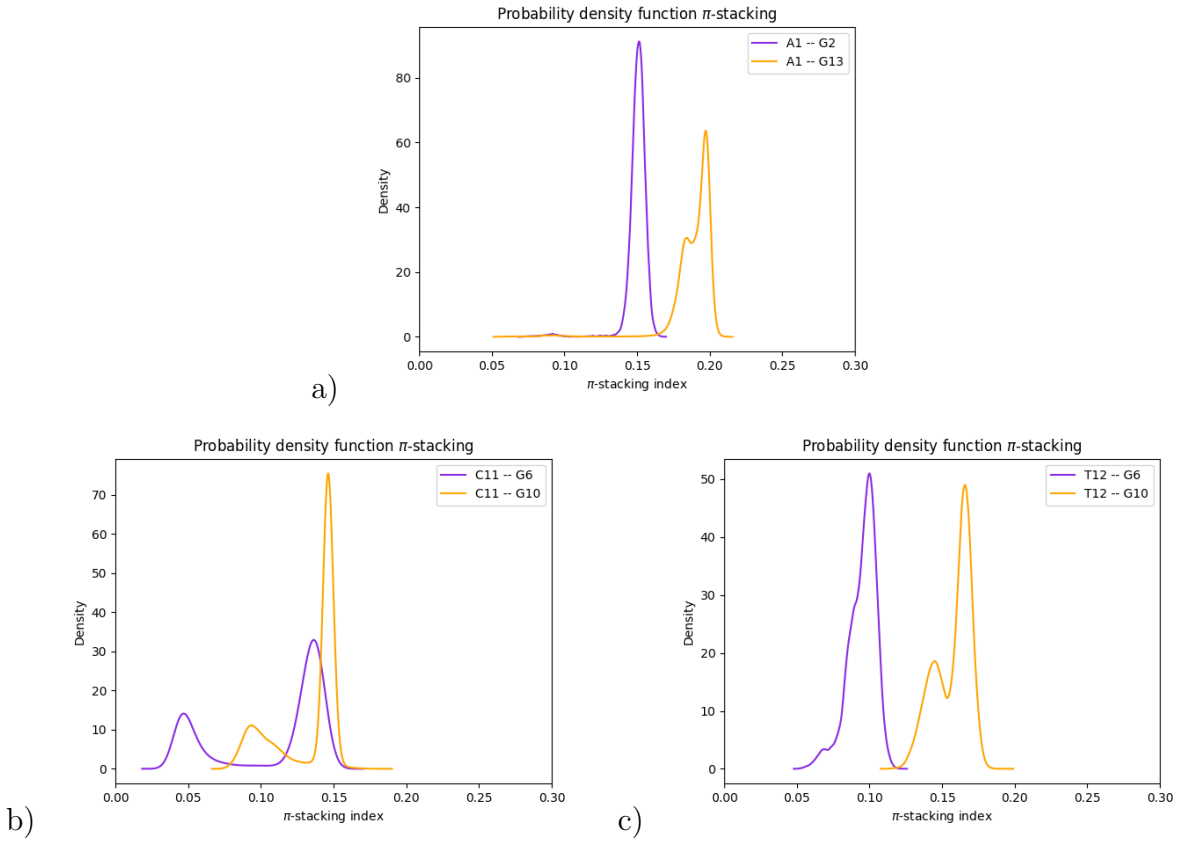

Figure 6: π-π stacking indexes for base pairs A1–G2, A1–G13, C11–G6, C11–G10, T12–G6 and T12–G10 calculated from the adaptive MD trajectories.

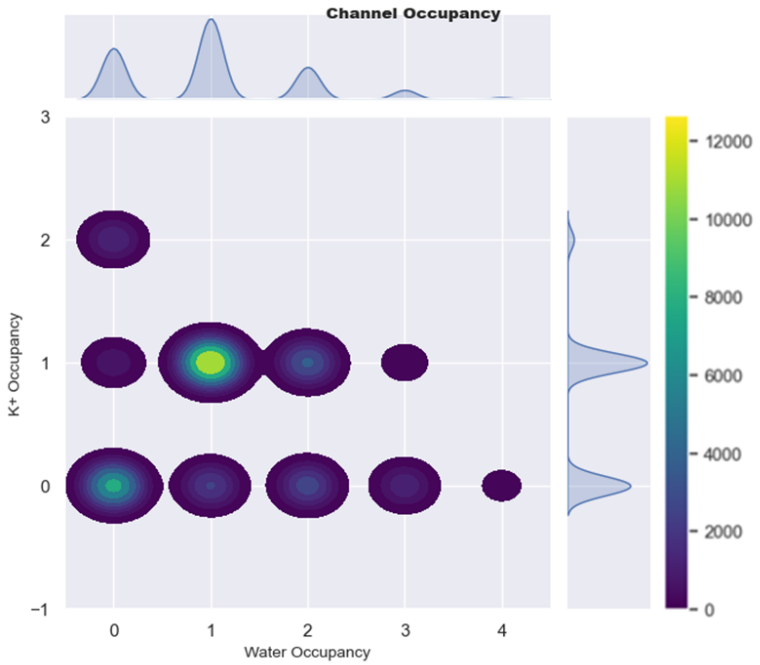

Figure 7: 2D probability density function representation of *c-kit1* GQ channel occupancy throughout the 20 independant trajectories of 20ns each starting from an empty channel. The color bar represents the frame density, from blue to yellow we represent respectively the lowest and the highest density region.

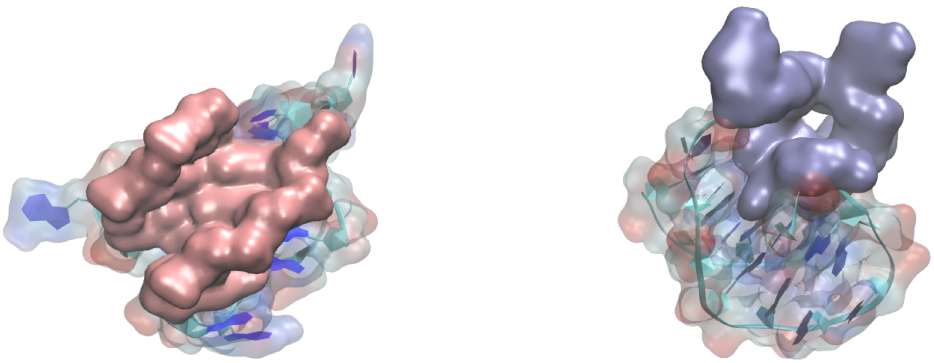

a) b)

Figure 8: Representation of the two cryptic pockets inside *c-kit1* GQ; a) P1 (pink color) formed by the bases A1, G2, G3, G13, G14, G15, A16, and b) P2 (ice blue) formed by bases G7, G8, C9, G10, C11, G21.

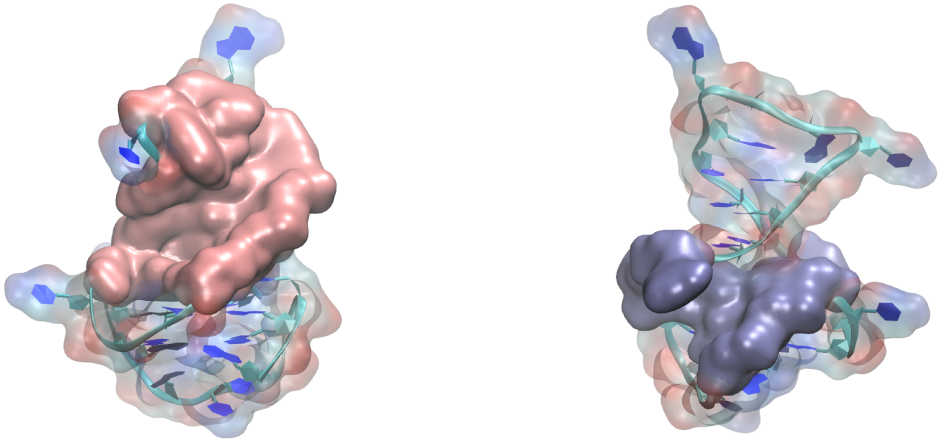

a) b)

Figure 9: Representation of the two cryptic pockets inside LTR-III HIV GQ structure c) P1 (pink color) is formed by the hairpin residues and d) P2 (iceblue) is formed by the GQ core bases.

Acknowledgement

DEA thanks funding from the Lebanese National Council for Scientific Research, CNRS-L. FC thanks funding from the French state funds managed by the CalSimLab LABEX and the ANR within the Investissements d'Avenir program (reference ANR11-IDEX-0004-02) and support from the Direction Génerale de l'Armement (DGA) Maîtrise NRBC of the French Ministry of Defense. This work was also made possible thanks to funding from the European Research Council (ERC) under the European Union's Horizon 2020 research and innovation program (grant agreement No 810367), project EMC2, JPP). Computations have been performed at GENCI (IDRIS, Orsay, France and TGCC, Bruyères le Chatel) on grant no A0130712052 (JPP).

Supporting Information Available

Supplementary information is available. It includes: the free energy values of each of the identified tICA clusters; the nucleotides probability density functions; the RMSF of ckit1 GQ components in each of identified tICA clusters.; the c-kit1 GQ RMSD for each of the 20 independent MD simulations starting from an empty ionic channel.

References

(1) Rhodes, D.; Lipps, H. J. G-quadruplexes and their regulatory roles in biology. *Nucleic Acids Res.* **2015**, *43*, 8627–8637.

(2) Balasubramanian, S.; Hurley, L. H.; Neidle, S. Targeting G-quadruplexes in gene promoters: a novel anticancer strategy? *Nature Reviews Drug Discovery* **2011**, *10*, 261–275.

(3) Hardin, C. C.; Watson, T.; Corregan, M.; Bailey, C. Cation-dependent transition be-

tween the quadruplex and Watson-Crick hairpin forms of d(CGCG3GCG). *Biochemistry* **1992**, *31*, 833–841.

(4) Li, W.; Wu, P.; Ohmichi, T.; Sugimoto, N. Characterization and thermodynamic properties of quadruplex/duplex competition. *FEBS letters* **2002**, *526*, 77–81.

(5) Simonsson, T. G-quadruplex DNA structures–variations on a theme. *Biol. Chem.* **2001**, *382*, 621–628.

(6) Burge, S.; Parkinson, G. N.; Hazel, P.; Todd, A. K.; Neidle, S. Quadruplex DNA: sequence, topology and structure. *Nucleic Acids Res* **2006**, *34*, 5402–5415.

(7) Phan, A. T.; Kuryavyi, V.; Burge, S.; Neidle, S.; Patel, D. J. Structure of an Unprecedented G-Quadruplex Scaffold in the Human c-kit Promoter. *J. Am. Chem. Soc.* **2007**, *129*, 4386–4392.

(8) Islam, B.; Stadlbauer, P.; Krepl, M.; Koca, J.; Neidle, S.; Haider, S.; Sponer, J. Extended molecular dynamics of a c-kit promoter quadruplex. *Nucleic Acids Res* **2015**, *43*, 8673–8693.

(9) Liu, L.; Bailey, S. M.; Okuka, M.; Muñoz, P.; Li, C.; Zhou, L.; Wu, C.; Czerwiec, E.; Sandler, L.; Seyfang, A.; Blasco, M. A.; Keefe, D. L. Telomere lengthening early in development. *Nat Cell Biol.* **2007**, *9*, 1436–41.

(10) Brooks, T. A.; Hurley, L. H. The role of supercoiling in transcriptional control of MYC and its importance in molecular therapeutics. *Nature Reviews Cancer* **2009**, *9*, 849–861.

(11) Heinrich, M. C. et al. Kinase mutations and imatinib response in patients with metastatic gastrointestinal stromal tumor. *J Clin Oncol.* **2003**, *21*, 4341–4349.

(12) Huppert, J. L.; Bugaut, A.; Kumari, S.; Balasubramanian, S. G-quadruplexes: the beginning and end of UTRs. *Nucleic Acids Res* **2008**, *36*, 6260–6268.

(13) Frolov, A.; Chahwan, S.; Ochs, M.; Arnoletti, J. P.; Pan, Z.-Z.; Favorova, O.; Fletcher, J.; von Mehren, M.; Eisenberg, B.; Godwin, A. K. Response Markers and the Molecular Mechanisms of Action of Gleevec in Gastrointestinal Stromal Tumors. *Mol Cancer Ther.* **2003**, *2*, 699–709.

(14) Foster, B. M.; Zaidi, D.; Young, T. R.; Mobley, M. E.; Kerr, B. A. CD117/c-kit in Cancer Stem Cell-Mediated Progression and Therapeutic Resistance. *biomedicines 6*.

(15) Babaei, M. A.; Kamalidehghan, B.; Saleem, M.; Huri, H. Z.; Ahmadipour, F. Receptor tyrosine kinase (c-Kit) inhibitors: a potential therapeutic target in cancer cells. *Drug Des Devel Ther* **2016**, *10*, 2443–2459.

(16) Hochhaus, A.; Larson, R. A.; Guilhot, F.; Radich, J. P.; Branford, S.; Hughes, T. P.; Baccarani, M.; Deininger, M. W.; Cervantes, F.; Fujihara, S.; Ortmann, C.-E.; Menssen, H. D.; Kantarjian, H.; O'Brien, S. G.; Druker, B. J. Long-Term Outcomes of Imatinib Treatment for Chronic Myeloid Leukemia. *N Engl J Med* **2017**, *376*, 917–927.

(17) Bhamidipati, P. K.; Kantarjian, H.; Cortes, J.; Cornelison, A. M.; Jabbour, E. Management of imatinib-resistant patients with chronic myeloid leukemia. *Therapeutic Advances in Hematology* **2013**, *4*, 103–117.

(18) Rankin, S.; Reszka, A. P.; Huppert, J.; Zloh, M.; Parkinson, G. N.; Todd, A. K.; Ladame, S.; Balasubramanian, S.; Neidle, S. Putative DNA Quadruplex Formation within the Human c-kit Oncogene. *J. Am. Chem. Soc.* **2005**, *127*, 10584–10589.

(19) Wei, D.; Husby, J.; Neidle, S. Flexibility and structural conservation in a c-KIT G-quadruplex. *Nucleic Acids Res* **2015**, *43*, 629–644.

(20) Wei, D.; Parkinson, G. N.; Reszka, A. P.; Neidle, S. Crystal structure of a c-kit promoter quadruplex reveals the structural role of metal ions and water molecules in maintaining loop conformation. *Nucleic Acids Res* **2012**, *40*, 4691–4700.

(21) Salsbury, A. M.; Lemkul, J. A. Molecular Dynamics Simulations of the c-kit 1 Promoter G-Quadruplex: Importance of Electronic Polarization on Stability and Cooperative Ion Binding. *J Phys Chem B.* **2019**, *123*, 148–159.

(22) Perrone, R.; Nadai, M.; Frasson, I.; Poe, J. A.; Butovskaya, E.; Smithgall, T. E.; Palumbo, M.; Palù, G.; Richter, S. N. A dynamic G-quadruplex region regulates the HIV-1 long terminal repeat promoter. *J Med Chem.* **2013**, *19*, 6521–6530.

(23) Piekna-Przybylska, D.; Sullivan, M. A.; Sharma, G.; Bambara, R. A. U3 region in the HIV-1 genome adopts a G-quadruplex structure in its RNA and DNA sequence. *Biochemistry.* **2014**, *16*, 2581–2593.

(24) Amrane, S.; Kerkour, A.; Bedrat, A.; Vialet, B.; Andreola, M.-L.; Mergny, J.-L. Topology of a DNA G-quadruplex structure formed in the HIV-1 promoter: a potential target for anti-HIV drug development. *J Am Chem Soc.* **2014**, *14*, 5249–5252.

(25) Zhang, C.; Lu, C.; Jing, Z.; Wu, C.; Piquemal, J.-P.; Ponder, J. W.; Ren, P. AMOEBA Polarizable Atomic Multipole Force Field for Nucleic Acids. *J. Chem. Theory Comput.* **2018**, *14*, 2084–2108.

(26) Shi, Y.; Ren, P.; Schnieders, M.; Piquemal, J.-P. *Reviews in Computational Chemistry Volume 28*; John Wiley and Sons, Ltd, 2015; Chapter 2, pp 51–86.

(27) Melcr, J.; Piquemal, J.-P. Accurate biomolecular simulations account for electronic polarization. *Front. Mol. Biosci.* **2019**, *6*, 143.

(28) Jing, Z.; Liu, C.; Cheng, S. Y.; Qi, R.; Walker, B. D.; Piquemal, J.-P.; Ren, P. Polarizable Force Fields for Biomolecular Simulations: Recent Advances and Applications. *Ann. Rev. Biophys.* **2019**, *48*, 371–394.

(29) Jaffrelot-Inizan, T.; Célerse, F.; Adjoua, O.; Ahdab, D. E.; Jolly, L.-H.; Montes, M.; Lagarde, N.; Ren, P.; Lagardère, L.; Monmarché, P.; Piquemal, J.-P. High-resolution

mining of the SARS-CoV-2 main protease conformational space: supercomputer-driven unsupervised adaptive sampling. *Chem. Sci.* **2021**, *12*, 4889–4907.

(30) El Ahdab, D.; Lagardère, L.; Jaffrelot Inizan, T.; Célerse, F.; Liua, C.; Adjoua, O.; Jolly, L.-H.; Gresh, N.; Hobaika, Z.; Ren, P.; Maroun, R. G.; Piquemal, J.-P. Interfacial Water Many-Body Effects Drive Structural Dynamics and Allosteric Interactions in SARS-CoV-2 Main Protease Dimerization Interface. *J. Phys. Chem. Lett.* **2021**, *12*, 6218–6226.

(31) El Khoury, L. et al. Computationally driven discovery of SARS-CoV-2 Mpro inhibitors: from design to experimental validation. *Chem. Sci.* **2022**, *13*, 3674–3687.

(32) Blazhynska, M.; Lagardère, L.; Liu, C.; Adjoua, O.; Ren, P.; Piquemal, J.-P. Water–glycan interactions drive the SARS-CoV-2 spike dynamics: insights into glycan-gate control and camouflage mechanisms. *Chem. Sci.* **2024**, DOI: 10.1039/D4SC04364B.

(33) Gresh, N.; Cisneros, G. A.; Darden, T. A.; Piquemal, J.-P. Anisotropic, Polarizable Molecular Mechanics Studies of Inter- and Intramolecular Interactions and Ligand-Macromolecule Complexes. A Bottom-Up Strategy. *Journal of Chemical Theory and Computation* **2007**, *3*, 1960–1986, PMID: 18978934.

(34) Gresh, N.; Naseem-Khan, S.; Lagardère, L.; Piquemal, J.-P.; Sponer, J. E.; Sponer, J. Channeling through Two Stacked Guanine Quartets of One and Two Alkali Cations in the Li+, Na+, K+, and Rb+ Series. Assessment of the Accuracy of the SIBFA Anisotropic Polarizable Molecular Mechanics Potential. *J. Phys. Chem. B* **2017**, *121*, 3997—-4014.

(35) Kruse, H.; Mladek, A.; Gkionis, K.; Hansen, A.; Grimme, S.; Sponer, J. Quantum Chemical Benchmark Study on 46 RNA Backbone Families Using a Dinucleotide Unit. *J. Chem. Theory Comput.* **2015**, *11*, 4972–4991.

(36) Adjoua, O.; Lagardère, L.; Jolly, L.-H.; Durocher, A.; Very, T.; Dupays, I.; Wang, Z.; Inizan, T. J.; Célerse, F.; Ren, P.; Ponder, J. W.; Piquemal, J.-P. Tinker-HP: Accelerating Molecular Dynamics Simulations of Large Complex Systems with Advanced Point Dipole Polarizable Force Fields Using GPUs and Multi-GPU Systems. *Journal of Chemical Theory and Computation* **2021**, *17*, 2034–2053, PMID: 33755446.

(37) Lagardère, L.; Jolly, L.-H.; Lipparini, F.; Aviat, F.; Stamm, B.; Jing, Z. F.; Harger, M.; Torabifard, H.; Cisneros, G. A.; Schnieders, M. J.; Gresh, N.; Maday, Y.; Ren, P. Y.; Ponder, J. W.; Piquemal, J.-P. Tinker-HP: a massively parallel molecular dynamics package for multiscale simulations of large complex systems with advanced point dipole polarizable force fields. *Chem. Sci.* **2018**, *9*, 956–972.

(38) Pérez-Hernández, G.; Paul, F.; Giorgino, T.; De Fabritiis, G.; Noé, F. Identification of slow molecular order parameters for Markov model construction. *J. Chem. Phys.* **2013**, *139*.

(39) Schwantes, C. R.; Pande, V. S. Improvements in Markov State Model Construction Reveal Many Non-Native Interactions in the Folding of NTL9. *J. Chem. Theory Comput.* **2013**, *9*, 2000–2009.

(40) Noé, F.; Nüske, F. A Variational Approach to Modeling Slow Processes in Stochastic Dynamical Systems. *Multiscale Model. Simul.* **2013**, *11*, 635–655.

(41) Nüske, F.; Keller, B. G.; Pérez-Hernández, G.; Mey, A. S. J. S.; Noé, F. Variational Approach to Molecular Kinetics. *J Chem Theory Comput.* **2014**, *8*, 1739–52.

(42) Branduardi, D.; Gervasio, F. L.; Cavalli, A.; Recanatini, M.; Parrinello, M. The role of the peripheral anionic site and cation-π interactions in the ligand penetration of the human AChE gorge. *J. Am. Chem. Soc.* **2005**, *127*, 9147–9155.

(43) Volkamer, A.; Kuhn, D.; Rippmann, F.; Rarey, M. DoGSiteScorer: a web server for au-

tomatic binding site prediction, analysis and druggability assessment. *Bioinformatics.* **2012**, *28*, 2074–2075.

(44) Jaffrelot-Inizan, T.; Célerse, F.; Adjoua, O.; El Ahdab, D.; Jolly, L.-H.; Liu, C.; Ren, P.; Montes, M.; Lagarde, N.; Lagardère, L.; Monmarché, P.; Piquemal, J.-P. High-Resolution Mining of SARS-CoV-2 Main Protease Conformational Space: Supercomputer-Driven Unsupervised Adaptive Sampling. *Chem. Sci.* **2021**, *12*, 4889–4907.

(45) Ponder, J. W.; Wu, C.; Ren, P.; Pande, V. S.; Chodera, J. D.; Schnieders, M. J.; Haque, I.; Mobley, D. L.; Lambrecht, D. S.; DiStasio, R. A.; Head-Gordon, M.; Clark, G. N. I.; Johnson, M. E.; Head-Gordon, T. Current Status of the AMOEBA Polarizable Force Field. *J. Phys. Chem. B* **2010**, *114*, 2549–2564.

(46) Shi, Y.; Xia, Z.; Zhang, J.; Best, R.; Wu, C.; Ponder, J. W.; Ren, P. Polarizable Atomic Multipole-Based AMOEBA Force Field for Proteins. *J. Chem. Theory Comput.* **2013**, *9*, 4046–4063.

(47) Rackers, J. A.; Wang, Z.; Lu, C.; Laury, M. L.; Lagardère, L.; Schnieders, M. J.; Piquemal, J.-P.; Ren, P.; Ponder, J. W. Tinker 8: Software Tools for Molecular Design. *J. Chem. Theory and Comput.* **2018**, *14*, 5273–5289.

(48) Lagardère, L.; Lipparini, F.; Polack, ; Stamm, B.; Cancès, ; Schnieders, M.; Ren, P.; Maday, Y.; Piquemal, J.-P. Scalable Evaluation of Polarization Energy and Associated Forces in Polarizable Molecular Dynamics: II. Toward Massively Parallel Computations Using Smooth Particle Mesh Ewald. *Journal of Chemical Theory and Computation* **2015**, *11*, 2589–2599, PMID: 26575557.

(49) Bowman, G. R.; Ensign, D. L.; Pande, V. S. Enhanced Modeling via Network Theory: Adaptive Sampling of Markov State Models. *J. Chem. Theory. Comput.* **2010**, *6*, 787–794.

(50) Zimmerman, M. I.; Porter, J. R.; Sun, X.; Silva, R. R.; Bowman, G. R. Choice of Adaptive Sampling Strategy Impacts State Discovery, Transition Probabilities, and the Apparent Mechanism of Conformational Changes. *J. Chem. Theory. Comput.* **2018**, *14*, 5459–5475.

(51) Betz, R. M.; Dror, R. O. How Effectively Can Adaptive Sampling Methods Capture Spontaneous Ligand Binding? *J. Chem. Theory. Comput.* **2019**, *15*, 2053–2063.

(52) Hruska, E.; Abella, H. R.; Nüske, F.; Kavraki, L. E.; Clementi, C. Quantitative comparison of adaptive sampling methods for protein dynamics. *J. Chem. Phys.* **2018**, *149*, 244119.

(53) Célerse, F.; Inizan, T. J.; Lagardère, L.; Adjoua, O.; Monmarché, P.; Miao, Y.; Derat, E.; Piquemal, J.-P. An Efficient Gaussian-Accelerated Molecular Dynamics (GaMD) Multilevel Enhanced Sampling Strategy: Application to Polarizable Force Fields Simulations of Large Biological Systems. *Journal of Chemical Theory and Computation* **2022**, *18*, 968–977, PMID: 35080892.

(54) Naritomi, Y.; Fuchigami, S. Slow dynamics of a protein backbone in molecular dynamics simulation revealed by time-structure based independent component analysis. *J. Chem. Phys.* **2013**, *139*, 215102.